Image-domain waveform tomography with two-way wave-equation

Tongning Yang and Paul Sava, Center for Wave Phenomena, Colorado School of Mines*

SUMMARY

We propose an image-domain velocity model building method using the two-way wave equation and extended seismic images. We show that common-image-point gathers can effectively extract velocity information from steep reflections imaged with the two-way wave propagator. Such gathers have the advantages over conventional common-image gathers that they are capable of characterizing reflections with arbitrary dip and that they are computationally cheap especially for wide-azimuth imaging. We develop a waveform tomography procedure based on the adjoint-state method and common-image-point gathers. Synthetic examples show that the information from steep reflections improve the resolution of velocity estimation, thus potentially leading to more accurate and faster converging inversion.

INTRODUCTION

In seismic imaging, building an accurate and reliable velocity model remains one of the biggest challenges. The need for high-quality velocity models is driven by the wide spread use of advanced imaging techniques such as one-way wave-equation migration (WEM) and reverse-time migration (RTM) because these migration methods are highly sensitive to the quality of the velocity model (Etgen et al., 2009).

In the past decade, velocity model building methods using full seismic wavefields (Vigh and Starr, 2008; Symes, 2009) have been gaining momentum, mainly due to their accuracy and to advances in computing technology. The family of such velocity estimation techniques can be categorized into data-domain methods (Sirgue and Pratt, 2004; Plessix, 2009) and image-domain methods (Sava and Biondi, 2004a; Shen and Symes, 2008).

Conventional wave-equation-based image-domain approaches use the one-way wave-equation as the engine to construct the image and to compute the gradient of the objective function. The input for this category of methods are various types of common-image gathers (CIGs) which serve as the foundation of the optimization problem defined using the semblance principle. The gathers are usually constructed as functions of depth and redundant parameters such as space-lag (Rickett and Sava, 2002; Shen and Calandra, 2005), time-lag (Sava and Fomel, 2006; Yang and Sava, 2010), or reflection angle (Sava and Fomel, 2003; Sava and Biondi, 2004b).

With the recent developments in forward modeling and computing hardware, RTM has become common for imaging applications, especially in complex subsurface areas. Using a two-way wave-equation propagator, one can better approximates the wave propagation in subsurface for velocity estimation process (Mulder, 2008). Furthermore, the capability of RTM for imaging steep reflections benefits velocity model building since information can be extracted from the image to constrain the velocity updates (Gao and Symes, 2009). To effectively access the velocity information contained in steep reflections, conventional CIGs are replaced by common-image-point gathers (CIPs) (Sava and Vasconcelos, 2011) for two reasons. First, CIPs avoid the directional bias towards horizontal reflections, and thus they take advantage of the steep dips obtained by RTM. Secondly, the sparse spatial sampling of CIPs reduces the computational cost and storage requirements.

In this paper, we propose an image-domain wavefield-based velocity model building approach and refer to this method as image-domain waveform tomography (WET) as a companion of data-domain tomography known as full waveform inversion (FWI). One key component of image-domain WET is wavefield simulation using a two-way wave-equation engine, similar to FWI. Another key component of the method is the objective function (OF) which is constructed by applying a penalty operator to CIPs whose minimization allows us to optimize image coherency and to update the velocity model. The third component is an effective gradient calculation based on the adjoint state method (Plessix, 2006; Symes, 2009). In summary, this computation consists of the following steps: (1) compute the *state variables*, i.e. the seismic wavefields obtained from the source by forward modeling and from the data by backward modeling; (2) compute the *adjoint source*, i.e. a calculation based on the OF and on the state variables; (3) compute the *adjoint state variables*, i.e. the seismic wavefields obtained from the adjoint source by backward modeling; (4) compute the *gradient* using the state and adjoint state variables.

This paper illustrates the workflow of image-domain WET implemented with CIPs. We show that using CIPs overcomes the bias toward nearly horizontal reflectors. More importantly, the information extracted from steep reflections provides more constraints on the velocity model and thus improves the convergence and resolution of the velocity estimation, as demonstrated by our synthetic example.

THEORY

We compute the gradient for image-domain WET, following the four steps of the adjoint-state method discussed in the preceding section.

The state variables relate the objective function to the model parameters. We use the seismic wavefields as the

state variables for image-domain WET:

$$\begin{bmatrix} \mathcal{L}(\mathbf{x},\omega,m) & 0 \\ 0 & \mathcal{L}^*(\mathbf{x},\omega,m) \end{bmatrix} \begin{bmatrix} u_s(\mathbf{e},\mathbf{x},\omega) \\ u_r(\mathbf{e},\mathbf{x},\omega) \end{bmatrix} = \begin{bmatrix} f_s(\mathbf{e},\mathbf{x},\omega) \\ f_r(\mathbf{e},\mathbf{x},\omega) \end{bmatrix} . \tag{1}$$

$\mathcal{L}$ and $\mathcal{L}^*$ denote the two-way wave operator and its adjoint in the frequency-domain, u_s and u_r are the simulated source and receiver wavefields, f_s and f_r are the source and record data, m are the model parameters, $\mathbf{e}$ is the experiment index, ω is the frequency, and $\mathbf{x}$ are the space coordinates $\{x, y, z\}$.

The adjoint sources are used to model the adjoint state variables, and these sources are computed based on the particular choice of the objective function and state variables. The OF for image-domain WET is formulated to minimize image inconsistencies caused by the model errors. Thus, the optimization process simultaneously improves the model and the image quality. We consider the objective function in the $\boldsymbol{\lambda} - \tau$ domain:

$$\mathcal{H}_{\boldsymbol{\lambda},\tau} = \frac{1}{2} \| K_I(\mathbf{x})\, P(\boldsymbol{\lambda},\tau)\, r(\mathbf{x},\boldsymbol{\lambda},\tau) \|^2_{\mathbf{x},\boldsymbol{\lambda},\tau} , \tag{2}$$

which uses the extended image

$$\begin{aligned} r(\mathbf{x},\boldsymbol{\lambda},\tau) &= \sum_{\mathbf{e}} \sum_{\omega} \overline{u_s(\mathbf{e},\mathbf{x}-\boldsymbol{\lambda},\omega)} u_r(\mathbf{e},\mathbf{x}+\boldsymbol{\lambda},\omega)\, e^{2i\omega\tau} \\ &= \sum_{\mathbf{e}} \sum_{\omega} T(-\boldsymbol{\lambda})\, \overline{u_s(\mathbf{e},\mathbf{x},\omega)} T(\boldsymbol{\lambda})\, u_r(\mathbf{e},\mathbf{x},\omega)\, e^{2i\omega\tau} . \end{aligned} \tag{3}$$

The operator $T(\boldsymbol{\lambda})$ represents the space shift applied to the wavefields in such a way that

$$T(\boldsymbol{\lambda})\, u(\mathbf{e},\mathbf{x},\omega) = u(\mathbf{e},\mathbf{x}+\boldsymbol{\lambda},\omega) . \tag{4}$$

The masking operator $K_I(\mathbf{x})$ restricts the construction of extended images on sparse locations only, e.g. on reflectors where we evaluate the accuracy of the velocity model. The penalty operator $P(\boldsymbol{\lambda},\tau)$ for vector lags is

$$P(\boldsymbol{\lambda},\tau) = \sqrt{|\boldsymbol{\lambda}\cdot\mathbf{q}|^2 + (V\tau)^2} . \tag{5}$$

Here $\mathbf{q}$ is the unit vector in the reflection plane and V represents the local migration velocity. Figure 1(a) and 1(b) show the penalty operators constructed using equation 5. Notice that the penalties for CIPs on vertical and horizontal reflections highlight the image inconsistencies in $h_z - \tau$ and $h_x - \tau$ panels, respectively.

The adjoint sources are computed as the derivatives of $\mathcal{H}_{\boldsymbol{\lambda},\tau}$ (equation 2) with respect to the state variables u_s and u_r, respectively:

$$\begin{aligned} g_s(\mathbf{e},\mathbf{x},\omega) &= K_I(\mathbf{x})\, \overline{K_I(\mathbf{x})} \times \\ &\sum_{\boldsymbol{\lambda},\tau} T(-\boldsymbol{\lambda})\, P(\boldsymbol{\lambda},\tau)\, \overline{P(\boldsymbol{\lambda},\tau) r(\boldsymbol{\lambda},\tau)} T(\boldsymbol{\lambda})\, u_r(\mathbf{e},\mathbf{x},\omega)\, e^{-2i\omega\tau} , \\ g_r(\mathbf{e},\mathbf{x},\omega) &= K_I(\mathbf{x})\, \overline{K_I(\mathbf{x})} \times \\ &\sum_{\boldsymbol{\lambda},\tau} T(\boldsymbol{\lambda})\, P(\boldsymbol{\lambda},\tau)\, \overline{P(\boldsymbol{\lambda},\tau)} r(\boldsymbol{\lambda},\tau)\, T(-\boldsymbol{\lambda})\, u_s(\mathbf{e},\mathbf{x},\omega)\, e^{-2i\omega\tau} . \end{aligned} \tag{6}$$

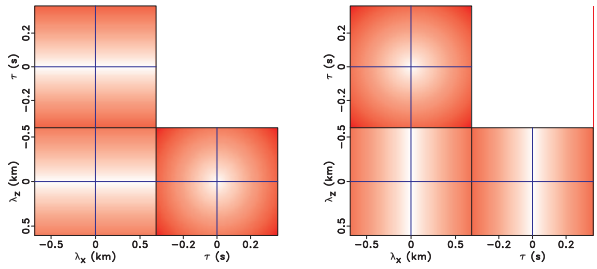

Figure 1: The penalty operators for (a) CIPs on vertical reflectors, and (b) CIPs on horizontal reflectors.

The adjoint state variable a_s and a_r are the wavefields obtained by backward and forward modeling using the corresponding adjoint sources:

$$\begin{bmatrix} \mathcal{L}^*(\mathbf{x},\omega,m) & 0 \\ 0 & \mathcal{L}(\mathbf{x},\omega,m) \end{bmatrix} \begin{bmatrix} a_s(\mathbf{e},\mathbf{x},\omega) \\ a_r(\mathbf{e},\mathbf{x},\omega) \end{bmatrix} = \begin{bmatrix} g_s(\mathbf{e},\mathbf{x},\omega) \\ g_r(\mathbf{e},\mathbf{x},\omega) \end{bmatrix} . \tag{7}$$

The computation of the gradient is simply a correlation of the state and adjoint-state variables:

$$\frac{\partial \mathcal{H}_{\boldsymbol{\lambda},\tau}}{\partial m} = \sum_{\mathbf{e}} \sum_{\omega} \frac{\partial \mathcal{L}}{\partial m} \left(u_s(\mathbf{e},\mathbf{x},\omega)\, \overline{a_s(\mathbf{e},\mathbf{x},\omega)} + u_r(\mathbf{e},\mathbf{x},\omega)\, \overline{a_r(\mathbf{e},\mathbf{x},\omega)} \right) . \tag{8}$$

If $\mathcal{L}$ is the Helmholtz wave operator $-\omega^2 m - \Delta$ where m is slowness square, then $\frac{\partial \mathcal{L}}{\partial m}$ is simply $-\omega^2$. This is similar to the analogous calculation in FWI (Pratt, 1999).

EXAMPLES

We illustrate our method with the synthetic model shown in Figure 2(a). The model consists of a smooth $v(z)$ background, a Gaussian low velocity variation, and a high velocity block with a vertical interface. Figures 2(b) and 2(c) show the image migrated using RTM with correct and incorrect velocities, respectively. The incorrect model is the smooth $v(z)$ background model. We construct the horizontal space-lag CIGs at locations indicated by the vertical lines at $x = 1$ km and $x = 2.5$ km in Figures 2(b) and 2(c). Figures 3(a) - 3(b) and Figures 3(c) - 3(d) show the gathers at $x = 1$ km and $x = 2.5$ km for correct and incorrect velocities, respectively. The gathers in Figure 3(c) and 3(d) are well behaved showing focused reflections or clear residual moveout. However, the gathers in Figure 3(a) and 3(b) are contaminated by artifacts as we construct the gathers with horizontal lags for vertical reflections. Thus, the reflections in the gathers are not correctly characterized and the CIGs in this case cannot provide velocity information.

For comparison, we construct the CIPs on locations indicated by the dots in Figures 2(b) and 2(c). Figures 4(a)

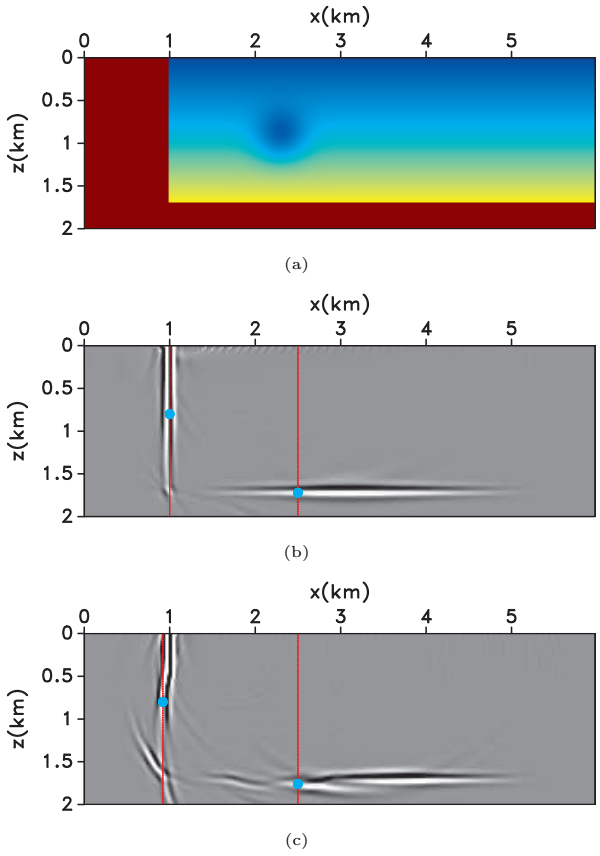

Figure 2: (a) The true velocity model. The images migrated with (b) the true velocity model, and (c) the incorrect velocity model.

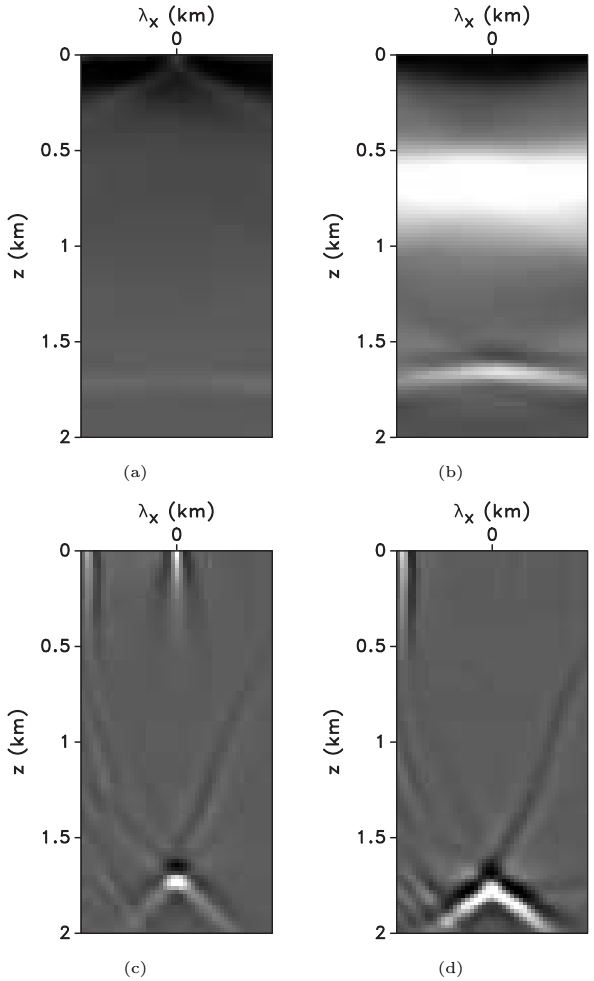

Figure 3: The space-lag CIGs at x=1 km migrated with (a) the correct velocity, (b) the incorrect velocity, and CIGs at x=2.5 km migrated with (c) the correct velocity, (d) the incorrect velocity.

- 4(b) and Figures 4(c) - 4(d) show the CIPs sampled on the vertical and horizontal reflector for the correct and incorrect velocities, respectively. The gathers in Figures 4(a) - 4(b) are constructed on the vertical reflector, and one can evaluate the model accuracy in the $h_z - \tau$ panel. The vertical reflection is correctly characterized with vertical space-lags, as the focus and residual moveout are observed in correct and incorrect velocities, respectively. On the other hand, the gathers in Figures 4(c) - 4(d), which are constructed on horizontal reflections, show well-behaved reflections in $h_x - \tau$ panel. The reflection is focused for the correct velocity and the residual moveout can be observed in the incorrect velocity. In these two extreme situations, CIPs are robust and able to correctly characterize reflections. The vector space-lags and time-lag in CIPs prevents the directional bias toward horizontal reflectors. Thus, CIPs allow us to analyze the velocity information from reflections with arbitrary dip.

Next, we demonstrate the implementation of image-domain WET and its advantages using the same synthetic model. Figure 5(a) plots the low velocity Gaussian variation which is the difference between the correct and incorrect migration velocities. The image obtained with the incorrect velocity is shown in Figure 2(c). Using the workflow introduced in the preceding sections, we compute the CIPs on the reflectors, and construct the objective function using equation 2. We then calculate the gradients in three different scenarios: using CIPs on the horizontal reflector only, using CIPs on the vetical reflector only, and using CIPs on both the horizontal and the vertical reflectors. Figure 5(b) and 5(c) show the gradient computed from CIPs on horizontal and vertical reflectors, respectively. We can observe that the gradients highlight the target in different ways. The gradient in Figure 5(b) constrains well the variation in the horizontal direction. In contrast, the gradient in Figure 5(c) constrains the variation in the vertical direction, but not the in horizontal direction. When the gradient is computed from CIPs on both vertical and horizontal reflectors, as shown in Figure 5(d), the variation is better controlled in both vertical and horizontal directions. We expect an inversion process implemented with this gradient to converge faster and result in a higher resolution velocity update.

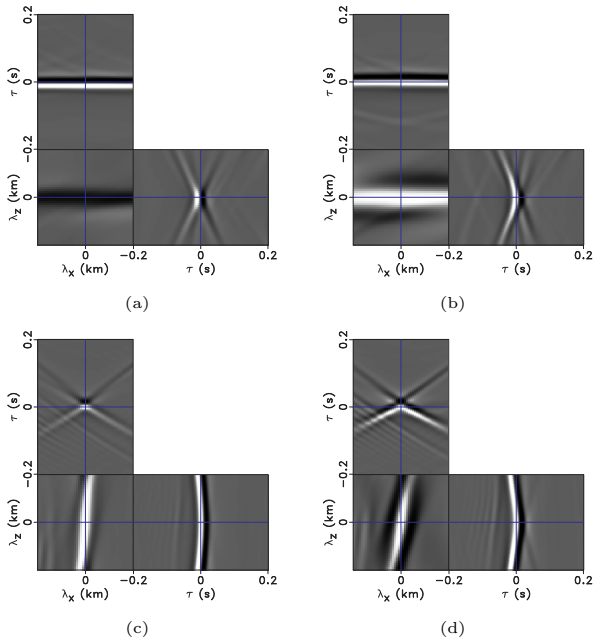

Figure 4: The CIPs at x=1 km, z=0.8 km migrated with (a) the correct velocity, (b) the incorrect velocity, and CIPs at x=1.7 km, z=2.5 km migrated with (c) the correct velocity, (d) the incorrect velocity.

CONCLUSIONS

We develop an image-domain waveform tomography approach with the wave propagation engine based on the two-way wave-equation. Steep reflections can be well imaged and provide additional information about the velocity model. CIPs are able to handle reflections with arbitrary dip and they benefit from using the two-way engine. The two-way wave propagator not only helps extract more velocity information, but it also constrains the model by using more complex wave phenomena such as diving waves. Synthetic examples show that the information from steep reflections can be effectively used and that the additional constraints have the potential to improve both the convergence and the resolution of wavefield-based velocity updates.

ACKNOWLEDGMENTS

This work was supported by the sponsors of the Consortium Project on Seismic Inverse Methods for Complex Structures at the Center for Wave Phenomena. The reproducible numeric examples in this paper use the Madagascar open-source software package freely available from http://www.reproducibility.org.

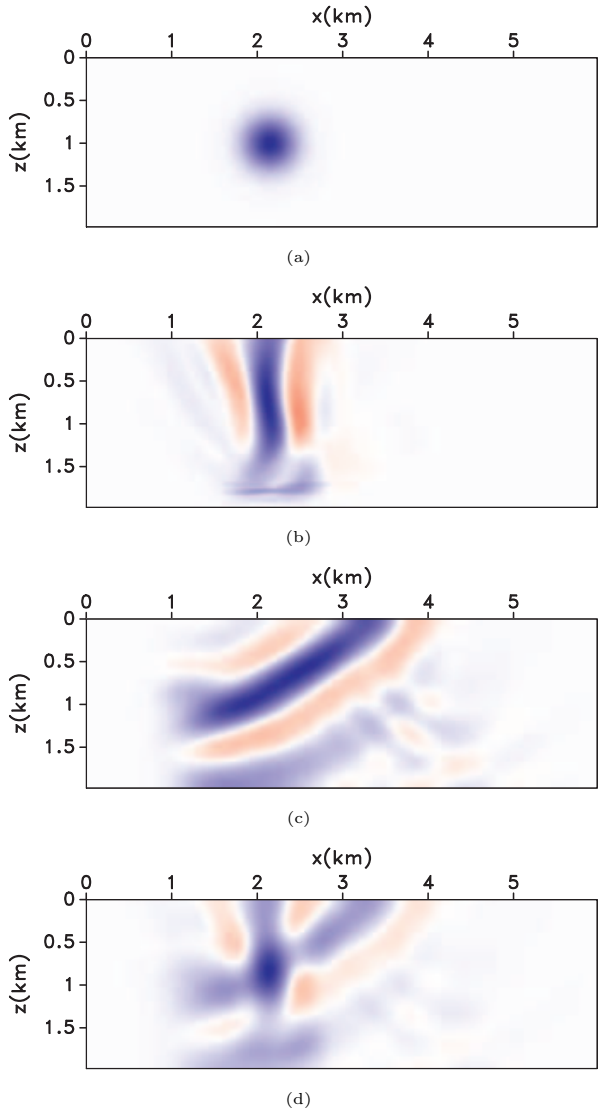

Figure 5: (a) The true velocity variation which is the target of inversion. The gradient constructed from (b) CIPs on the horizontal reflector only, (c) CIPs on the vertical reflector only, (d) CIPs on both the horizontal and vertical reflectors.

REFERENCES

Etgen, J., S. H. Gray, and Y. Zhang, 2009, An overview of depth imaging in exploration geophysics: Geophysics, **74**, WCA5–WCA17.

Gao, F., and W. Symes, 2009, Differential semblance velocity analysis by reverse time migration: Image gathers and theory: 77th Annual International Meeting, SEG, Expanded Abstracts, 2317–2320.

Mulder, W. A., 2008, Automatic velocity analysis with the two-way wave equation: Presented at the 70th EAGE Conference and Exhibition, Extended Abstracts.

Plessix, R.-E., 2006, A review of the adjoint state method for computing the gradient of a functional with geophysical applications: Geophysical Journal International, **167**, 495–503.

———, 2009, Three-dimensional frequency-domain full-waveform inversion with an iterative solver: Geophysics, **74**, WCC53–WCC61.

Pratt, R. G., 1999, Seismic waveform inversion in the frequency domain, Part 1: Theory and verification in a physical scale model: Geophysics, **64**, 888–901.

Rickett, J., and P. Sava, 2002, Offset and angle-domain common image-point gathers for shot-profile migration: Geophysics, **67**, 883–889.

Sava, P., and B. Biondi, 2004a, Wave-equation migration velocity analysis - I: Theory: Geophysical Prospecting, **52**, 593–606.

———, 2004b, Wave-equation migration velocity analysis - II: Subsalt imaging examples: Geophysical Prospecting, **52**, 607–623.

Sava, P., and S. Fomel, 2003, Angle-domain common image gathers by wavefield continuation methods: Geophysics, **68**, 1065–1074.

———, 2006, Time-shift imaging condition in seismic migration: Geophysics, **71**, S209–S217.

Sava, P., and I. Vasconcelos, 2011, Extended imaging condition for wave-equation migration: Geophysical Prospecting, **59**, 35–55.

Shen, P., and H. Calandra, 2005, One-way waveform inversion within the framework of adjoint state differential migration: 75th Annual International Meeting, SEG, Expanded Abstracts, 1709–1712.

Shen, P., and W. W. Symes, 2008, Automatic velocity analysis via shot profile migration: Geophysics, **73**, VE49–VE59.

Sirgue, L., and R. Pratt, 2004, Efficient waveform inversion and imaging: A strategy for selecting temporal frequencies: Geophysics, **69**, 231–248.

Symes, W., 2009, Migration velocity analysis and waveform inversion: Geophysical Prospecting, **56**, 765–790.

Vigh, D., and E. W. Starr, 2008, 3D prestack plane-wave, full-waveform inversion: Geophysics, **73**, VE135–VE144.

Yang, T., and P. Sava, 2010, Wave-equation migration velocity analysis with time-lag imaging: Geophysical Prospecting, submitted for publication.